Aqueous-phase chemistry of glyoxal with multifunctional reduced nitrogen compound: A potential missing route of secondary brown carbon

Yuemeng Ji[1,2], Zhang Shi[1,2], Wenjian Li[1,2], Jiaxin Wang[1,2], Qiuju Shi[1,2], Yixin Li[3], Lei Gao[1,2], Ruize Ma[1,2], Weijun Lu[2], Lulu Xu[1,2], Yanpeng Gao[1,2], Guiying Li[1,2], Taicheng An[1,2]

[1]Guangdong Key Laboratory of Environmental Catalysis and Health Risk Control, Guangdong-Hong Kong-Macao Joint Laboratory for Contaminants Exposure and Health, Institute of Environmental Health and Pollution control, Guangdong University of Technology, Guangzhou 510006, China;
[2]Guangzhou Key Laboratory of Environmental Catalysis and Pollution Control, Key Laboratory of City Cluster Environmental Safety and Green Development, School of Environmental Science and Engineering, Guangdong University of Technology, Guangzhou 510006, China.
[3]Department of Chemistry, University of California Irvine, Irvine, CA 92697, USA

Correspondence to: Prof. Taicheng An (antc99@gdut.edu.cn)

Abstract. Aqueous-phase chemistry of glyoxal (GL) with reduced nitrogen compounds (RNCs) plays a significant source of secondary brown carbon (SBrC), which is one of the largest uncertainties in climate predictions. However, few studies have revealed that SBrC formation is affected by multifunctional RNCs, which has a non-negligible atmospheric abundance. Hence, we performed theoretical and experimental approaches to investigate the reaction mechanisms and kinetics of the mixtures for ammonium sulfate (AS), multifunctional amine (monoethanolamine, MEA) and GL. Our experiments indicate that the light-absorption and the growth rate are enhanced in MEA-GL mixture relative to AS-GL and MEA-AS-GL mixtures, and MEA reactions of the chromophores by more efficiently than the analogous AS reactions. Quantum chemical calculations show that the formation and propagation of oligomers proceed via four-step nucleophilic addition reactions in three reaction systems. The presence of MEA provides the extra two branched chains to affect the natural charges and steric hindrance of intermediates, facilitated the formation of chromophores. Molecule dynamics simulations reveal that the interfacial and interior attraction on the aqueous aerosols with MEA is more pronounced for small α-dicarbonyls, to facilitate the further engagement in the aqueous-phase reactions. Our results show a possible missing source for SBrC formation on urban, regional and global scales.

1 Introduction

Brown carbon (BrC) represents the most important source of carbonaceous aerosols, with profound implications to the global climate, air quality and human health (Laskin et al., 2015; Marrero-Ortiz et al., 2018; Li et al., 2022; Yan et al., 2018; Yuan et al., 2023). Chemical transport models reveal that a non-negligible radiative forcing by BrC is range from 0.05 to 0.27 W m^{-2} averaged globally (Tuccella et al., 2020; Wang et al., 2018; De Haan et al., 2020; Zhang et al., 2020; Laskin et al., 2015; Moise et al., 2015). Large differences in these estimated data result from the uncertainties of BrC on its formation mechanisms,

chemical composition and optical properties (An et al., 2019; Shi et al., 2020; Kasthuriarachchi et al., 2020; Corbin et al., 2019). It affects understanding the radiative effect in current climate models (Liu et al., 2020; Zhang et al., 2020; Zhang et al., 2023). Compared with primary BrC, sources and formation of secondary BrC (SBrC) are more complex and lack of understanding in detail (Lin et al., 2015; Yuan et al., 2020; Srivastava et al., 2022). Hence, in recent years, great efforts have been made to better understand the chemical composition and formation mechanisms of SBrC chromophores.

There is compelling evidence that the heterogeneous reactions of reduced nitrogen compounds (RNCs) and small α-dicarbonyls have been recognized as significant sources of SBrC (Hawkins et al., 2018; De Haan et al., 2018; George et al., 2015). These SBrC chromophores are normally conjugated and possibly heteroaromatic species, such as imidazole (IML) and its derivatives (De Haan et al., 2009b; De Haan et al., 2009a; Yang et al., 2022). Numerous previous studies paid much attention to BrC from the secondary processes of small α-dicarbonyls with ammonium sulfate (AS) and methylamine (MA) (De Haan et al., 2020; De Haan et al., 2019; De Haan et al., 2009a; Lin et al., 2015). For example, nearly 30 chromophores were detected in AS-methylglyoxal (MG) mixture by HPLC/PDA/HRMS and nitrogen-containing compounds account for more than 70% of the overall light absorption within 300−500 nm range (Lin et al., 2015). Some studies have also revealed that the absorption of BrC generated in AS- or MA-MG mixture increases with pH value (Hawkins et al., 2018; Sedehi et al., 2013) Also, the iminium pathway is predominant while pH < 4 to form IML and its derivatives but is suppressed at pH 4.(Nozière et al., 2009; Sedehi et al., 2013; Yu et al., 2011). Hence, pH value has a large effect on the formation of SBrC chromophores, but the chemical mechanisms of BrC formation under the different pH values remain unclear, hindering a systematical understanding its integrated atmospheric chemistry and nonnegligible environmental impacts.

On the other hand, multifunctional RNCs (such as ethanolamines and amino acids) display a strong atmospheric activity to the formation of SBrC with an unneglected atmospheric concentration (Huang et al., 2016; Ge et al., 2011; Powelson et al., 2014b; Trainic et al., 2012; Laskin et al., 2015; Ning et al., 2022). For example, a rapid BrC formation was detected in glycine reactions with small α-dicarbonyls, and sub-micrometer amino acids particles exhibited a high growth upon exposure to small α-dicarbonyls (Powelson et al., 2014b; Sedehi et al., 2013; De Haan et al., 2009b; Trainic et al., 2012). On the other hand, monoethanolamine (MEA) is an amine-based solvent for post-combustion CO_2 capture (PCCC) technology with a relatively high vapor pressure, emitting 80 tons per year into the atmosphere for each 1 million tons of CO2 removed per year (Karl et al., 2011; Puxty et al., 2009; Shen et al., 2019). Recent field measurement has shown that MEA is the second most abundant organic amine in PM2.5 in Shanghai besides MA (Huang et al., 2016). However, to the best of our knowledge, few previous results are available on the participation of MEA in the SBrC formation with small α-dicarbonyls and its potential role in the atmosphere and human health were also not attempted.

Hence, we elucidated the chemical mechanisms of BrC chromophores from the mixtures of typical reaction of RCNs (i.e., MEA and AS) with small α-dicarbonyls using combined theoretical and experimental methods. Herein, glyoxal (GL) is selected as the representative of small α-dicarbonyls due to its high global emissions and significant contribution to BrC (Fu et al., 2008; Myriokefalitakis et al., 2008; Shi et al., 2020; Nie et al., 2022; Gomez et al., 2015). The chemical composition of the BrC chromophores was characterized by mass spectrometry in different initial pH values, and the optical properties were

66 measured using UV-Vis spectrophotometry. Possible pathways were calculated using density functional theory, and the

67 mechanism of BrC chromophore formation was also simulated. The effects of multifunctional amine in formation of SBrC

68 chromophores were elaborated further. Additionally, the potential implications of multifunctional amine on climate radiative

69 forcing were stated and discussed briefly.

2 Experimental methods and theoretical calculations

2.1 Experimental section

72 The procedures of each experiment are summarized in Fig. S1. All reagents were used as described in Supporting Information

73 (SI). Three mixtures were prepared under atmospheric relevant aqueous conditions to generate SBrC: AS-GL, MEA-GL and

74 MEA-AS-GL. Briefly, AS-GL (1 M) mixture was prepared by adding AS to aqueous GL (in ultrapure water) for a final

75 concentration of 1 M of each reactant in the volumetric flasks. For the two MEA-containing mixtures, MEA was acidified with

76 diluted sulfuric acid (20%) to prevent GL from reacting with MEA in alkaline condition. The acidified MEA was then combined

77 with aqueous GL similar to that described for the AS-GL (1 M) mixture. All three solutions mentioned above were then diluted

78 to reach a final concentration of 1 M in three 50mL volumetric flasks. To explore the effects of pH values, three mixtures were

79 prepared with an initial pH values of 3 or 4 via addition of sulfuric acid (20%) or sodium hydroxide solution (2 M) prior to the

80 mixing of RNCs and GL (Kampf et al., 2016; Yu et al., 2011). Each mixture was transported into brown vials, which has been

81 proven to avoid the photolysis and light-induced reactions of light-absorbing products (Kampf et al., 2012), to guarantee

82 efficiently produce chromophores in droplet evaporation collecting on the timescales of seconds (Zhao et al., 2015; Lee et al.,

83 2014).

84 The absorption spectra of all mixtures were recorded by using an UV-Vis spectrophotometer (Agilent Cary 300, USA).

85 All experimental solutions were diluted by a factor of 200 or 400 before each measurement to avoid saturation of the absorption

86 peaks. The diluted samples were added into a quartz cuvette with 1 cm optical path length right away to prevent the diluted

87 samples from photolysis. The spectra recorded between 200 – 500 nm were shown in Fig. 1. And the blank experiments of GL

88 and RNCs solution were performed and presented in Fig. S2. The absorption spectra of all samples were measured with three

89 times. The wavelength-dependent mass absorption coefficients (MACs) of experimental solutions were calculated from initial

90 base-10 absorbance (A_{10}),

$$\text{MAC}(\lambda) = \frac{A_{10}^{\text{solution}}(\lambda) \times \ln(10)}{b \times C_{\text{mass}}}$$

92 where C_{mass} is the mass concentration of reactants and b is path length (Aiona et al., 2017; Chen and Bond, 2010). The different

93 dilution factors were normalized by using MAC formula.

94 Samples used for mass spectrometry analysis were diluted by a factor of 800 or 1000 followed by syringe filtration. The

95 filters were stored in brown chromatography injection vials to block the light. Ultra-performance liquid chromatography

96 coupled to hybrid Quadrupole-Exactive Orbitrap mass spectrometry (UPLC-Q-Orbitrap HRMS, Thermo Scientific™, USA)

97   (Wang et al., 2017) was employed to obtain structural data of chromophores in this study. MS^2 analysis were used for all

98   chromophores with a weight error of less than 10 ppm compared with the theoretical mass to obtain fragments information for

99   the identification of structure analysis. Detailed description of the mass spectrometry and chromatographic conditions are all

100   described in SI.

2.2 Quantum calculations and molecular dynamics simulations

102   Quantum chemical calculations were performed using the Gaussian 09 package (M. J.Frisch, 2013). Structures for all

103   stationary points (SPs), including reactants, intermediates, transient states (TSs), and products, were optimized using the hybrid

104   density functional of M06-2X method(Zhao and Truhlar, 2007) with 6-311G(d,p) basis set, i.e., at the M06-2X/6-311G(d,p)

105   level (Ji et al., 2017). The solvent effect was considered using the solvation model based on density (SMD) to simulate the

106   aqueous environment (Gao et al., 2016; Marenich et al., 2009). Harmonic frequency calculation was carried out at the same

107   level as structural optimization to verify whether SP is a TS (with one and only imaginary frequency) or a minimum (without

108   imaginary frequencies) (Ji et al., 2022). Intrinsic reaction coordinate calculation was performed to confirm that the TSs

109   connected with the corresponding reactants and products. Single point energy (SPE) calculation was executed using the M06-

110   2X method with a more flexible 6-311+G(3df,3pd) basis set to obtain more accurate potential energy surfaces (PESs). For the

111   pathways with TSs, the rate constants (k) were calculated via conventional transition state theory (TST) (Evans and Polanyi,

112   1935; Eyring, 1935; Galano and Alvarez-Idaboy, 2009; Gao et al., 2014). To simulate real atmospheric conditions in the

113   solution, the calculated k values were refined by solvent cage effects(Okuno, 1997) and diffusion-limited effects (Collins and

114   Kimball, 1949), of which the calculation details of diffusion-limited rate constant k_d can be seen in SI. For the pathways without

115   TSs, the corresponding k values are predominated by the diffusion-limit effect which equal to the diffusion-limited rate

116   constants.

117   Classical molecular dynamics (MD) was performed using NAMD package (Phillips et al., 2005) to simulate the

118   heterogeneous processes of GL from gas to the AS and MEA particles. The AS particle is composed of 39 SO_4^{2-}, 78 NH_4^+ and

119   2046 H_2O in a box size of $40 \times 40 \times 40$ $Å^3$, while the MEA particle consists of 39 MEA and 2036 H_2O. The 5 ns equilibration

120   at the time step of 1 fs was executed in the isothermal-isochoric (NVT) ensemble ($T = 298$ K) to ensure the thermodynamic

121   equilibrium of particles (Shi et al., 2020; Zhang et al., 2019). The MD simulation of 2 ns is run via the NVT ensemble. MEA

122   and GL were described using CHARMM force field (Jorgensen et al., 1996), and H_2O using TIP3P model (Martins-Costa et

123   al., 2012). The fixed charges on NH_4^+ and SO_4^{2-} are scaled by 0.75 to account for the electronic polarizability (Leontyev and

124   Stuchebrukhov, 2011; Mosallanejad et al., 2020). The periodic boundary conditions were selected for three dimensions. In

125   order to calculate the kinetic trajectories of GL from gas to two target particles, the free energy profile along the distance of

126   the center of mass between each particle and GL was calculated via umbrella sampling (Torrie and Valleau, 1977) and

127   weighted-histogram analysis method (Kumar et al., 1992) based on the above equilibrated molecular dynamics trajectories.

128   The bias potential force constant was equal to 10 kcal mol^{-1} $Å^{-2}$.

3 RESULTS AND DISCUSSION

3.1 Mass absorption coefficients of BrC chromophores

The mass absorption coefficients (MACs) identified in AS-GL, MEA-GL, and MEA-AS-GL mixtures at the initial pH of 3 and 4 (denoted as pH = 3 and pH = 4) are shown in Fig. S3. The maximum adsorption peaks locate at 207, 212, and 209 nm for AS-GL, MEA-GL, and MEA-AS-GL mixtures at pH = 3, respectively, and the corresponding location is not changed at pH = 4. The MAC values of the maximum adsorption peaks are in the range of 1080−17909 cm^2 g^{-1} for three mixtures. In addition, each mixture has an absorption peak between 285 - 324 nm (Fig. S4), with a range of 42 - 228 cm^2 g^{-1}, which are consistent with the MAC values measured by Powelson et al. at the reaction time of 4 days (Powelson et al., 2014a) but are smaller than the values measured by Zhao et al. with a long reaction time of 2 - 3 months (Zhao et al., 2015). The MAC values at 207 - 212 and 285 - 324 nm exhibit a similar trend (Fig. S4). Therefore, to easily compare the absorbance in three mixtures, we focus on the adsorption peaks in the range of 207 - 212 nm, which exhibits an obvious variation, and the effect of the initial pH on reaction systems is also discussed in this range. The MAC values at pH = 4 are higher than those at pH = 3 for three mixtures. For example, the MAC value in AS-GL mixture is 2037 cm^2 g^{-1} at pH = 4, which is almost twice higher than that at pH = 3. Hence, the initial pH values of solution mainly affect the MAC values rather than the locations of absorption peaks.

In order to explore the influence of the initial pH values on the MAC values, a comparison of MAC values at initial pH 3 and 4 is performed for all three mixtures (Fig. 1a).Fig. 1a shows a comparison of the MAC values of all three mixtures at the initial pH of 3 and 4. The MAC values of maximum adsorption peaks increase from AS-GL to MEA-GL to MEA-AS-GL mixture, ranging from 1080 to 6345 cm^2 g^{-1} at pH = 3 and 2037 to 7617 cm^2 g^{-1} at pH = 4. The highest MAC value of MEA-AS-GL is explained by the different initial total concentration of reactants (see in Method), since the initial concentration of AS and MEA in MEA-AS-GL mixture is twice times than that in MEA-GL or AS-GL mixture. In addition, the MAC value of maximum adsorption peak in MEA-AS-GL mixture is higher than the sum of those in MEA-GL and AS-GL mixtures, and the location of maximum absorption peak in MEA-AS-GL mixture is between those in MEA-GL and AS-GL mixtures. It implies that the extra chromophores are yielded in MEA-AS-GL mixture in addition to producing the same chromophores as AS-GL and MEA-GL mixtures.

To compare the formation rate of chromophore between the different mixtures, the growth rates (GRs) of the maximum absorption peaks as a function of reaction time is shown in Fig. 2. The trend of the GR variation with reaction time at pH = 3 is similar to that at pH = 4, while the GRs of three mixtures at pH = 4 are larger than those at pH = 3 at the beginning of the reactions. The GRs are nearly invariant after 6−9 days, implying that the chromophore formation for three mixtures is irreversible. MEA-AS-GL mixture exhibits the larger GRs than other mixtures at the beginning of reaction because of its higher initial concentration of reactants. As the reaction proceeds, the GRs of MEA-GL mixture are increased and finally larger than those of other mixtures. Hence, MEA reactions form the chromophores by more efficiently than the analogous AS reactions.

The GRs dependence of the pH values of three mixtures is also plotted as a function of reaction time as shown in Fig. 2. The pH values rapidly degrade within the first 2 days in three mixtures, which is the same trend as GRs that decrease by a

162 factor of more than 1−3 at pH = 3 and 4. This trend is explained by ambient pH values, since a known byproduct (i.e., formic

163 acid) is formed (De Haan et al., 2009b; De Haan et al., 2020; Galloway et al., 2009; Hamilton et al., 2013; Kampf et al., 2012;

164 Yu et al., 2011). Note that the trend of GRs shows a decrease from MEA-AS-GL, MEA-GL, to AS-GL mixtures at the beginning

165 of the reaction time, while the MAC values of MEA-GL mixture are larger than those of two mixtures accompanied by the

166 more rapid decrease of pH values in solution after the reaction is equilibrium (Figs. 1b and 2), suggesting that chromophore

167 formation of three mixtures depends on the ambient pH value..

3.2 Chemical composition characterization of BrC chromophores

169 The chemical composition characterization of formed BrC chromophore was conducted by UPLC-Q-Orbitrap HRMS. The

170 formulas, m/z values, characteristic fragments, and structures of chromophores and intermediates are identified based on

171 obtained mass spectrum data in AS-GL, MEA-GL, and MEA-AS -GL mixtures (Table S1). The corresponding MS and MS^2

172 spectra of chromophores and intermediates are exhibited in Figs. 3, S8-S12. For all mixtures, imidazole (IML) compounds are

173 identified with a characteristic peak at m/z 69.045 in MS^2 spectra. Therefore, various IML compounds are observed based on

174 several representative peaks at m/z 69.045, including imidazole (IML_{AS} and IML_{MEA}), imidazole-2-carboxaldehyde (IC_{AS} and

175 IC_{MEA}), and their hydrated forms (HIC_{AS} and HIC_{MEA}) for AS-GL and MEA-GL mixtures (Table S1, Figs. 3a-b and S8-S9).

176 For MEA-GL mixture, extra catenulate intermediates without IML-structure characteristics are obtained at m/z values of

177 102.055 and 120.065 (Table S1, Figs. 3a and S10), corresponding to $C_4H_7O_2N$ (IA_{MEA}) and $C_4H_9O_3N$ (AHA_{MEA} and ID_{MEA})

178 compounds, respectively. However, no catenulate intermediates in AS-GL mixture are observed in this study because of their

179 low concentrations and short lifetimes, although they are observed by previous studies using MS/AMS and ^1H nuclear magnetic

180 resonance spectroscopy (Galloway et al., 2009; Lee et al., 2013; Yu et al., 2011). In addition, as shown in Figs. 3b and S11,

181 some IML-based products at m/z values of 145.061, 135.066, and 193.072 were obtained in AS-GL mixture correspond to

182 hydrated N-glyoxal substituted imidazole (HGI_{AS}), 2,2'-biimidazole (BIM_{AS}), and its glyoxal substituted analog (GBI_{AS}),

183 respectively. As discussed above, an important distinction between AS-GL and MEA-GL mixtures is whether formation of

184 bicyclic IML products (Fig. 3a-b), indicating that the optical properties of chromophores are mainly determined by mono-

185 imidazole compounds rather than bicyclic IML compounds.

186 To further explore the difference of identified products in MEA-GL and AS-GL mixtures, the possible pathways leading

187 to the identified intermediates and chromophores are illustrated in Fig. 4, along with the reaction energies (ΔG_r) of all pathways

188 calculated at the M06-2X/6-311+G(3df,3pd)//M06-2X/6-311G(d,p) level. As shown in Fig. 4, the formation and propagation

189 of oligomers was proposed to proceed via four-step nucleophilic addition (NA) reactions. For MEA-GL mixture, three

190 catenulate intermediates (AHA_{MEA}, IA_{MEA}, and ID_{MEA}) are successively yielded by the nucleophilic attack of MEA at the

191 reactive carbonyl site via dehydration and hydration, with the total ΔG_r value of -7.8 kcal mol^{-1} (Fig. 4a). Subsequently, two-

192 step NA reactions between ID_{MEA} and MEA and between DI_{MEA} and GL-diol (DL), followed by protonation and dehydration,

193 yields two intermediates (HA_{MEA} and PIC_{MEA}) in sequence. Although the third NA reaction between DI_{MEA} and DL is

194 endothermic (ΔG_r = 12.7 kcal mol^{-1}), the total ΔG_r value of DI_{MEA} formation in MEA-GL mixture is -18.7 kcal mol^{-1} for

195   proceeding the NA reaction to yield PIC$_{MEA}$. Similarly, the formation of PIC$_{AS}$ in AS-GL mixture is also thermodynamically

196   feasible, with the total ΔG_r value of -10.9 kcal mol^{-1}. However, PIC$_{MEA}$ or PIC$_{AS}$ is thermodynamically unstable, since there

197   is a large exothermicity of the subsequent reaction pathway ($\Delta G_r = -78.6$ or -50.0 kcal mol^{-1}) for proceeding cyclization

198   leading to the formation of IC$_{MEA}$ or IC$_{AS}$. It should be noted that for AS-GL mixture, the fate of IC$_{AS}$ is dependent of the

199   competition between the pathways of hydration to yield HIC$_{AS}$ and NA reaction with DL to form BI$_{AS}$, while for MEA-GL

200   mixture, there are no nucleophilic sites of IC$_{MEA}$ for further oligomerization to form bicyclic IML compounds because IC$_{MEA}$

201   is imidazolium cation. Similarly, IC$_{MEA}$ also undergoes a hydration reaction to form HIC$_{MEA}$ with a similar structure to HIC$_{AS}$.

202   Subsequently, HIC$_{AS}$ and HIC$_{MEA}$ are decomposed to yield IML$_{AS}$ and IML$_{MEA}$, respectively, accompanied by the formation

203   of formic acid ($\Delta G_r = -10.2$ and -15.6 kcal mol^{-1}), which is the reason for the decrease in pH in Section 3.1. However, as a

204   reaction byproduct, formic acid hardly participates in the formation of light-absorbing products, so it has little influence on the

205   reaction mechanisms. Current results further explain our experimental results mentioned above that higher MAC and larger

206   GR values in MEA-GL mixture than that in AS-GL mixture.

207   For MEA-AS-GL mixture, the products in AS-GL and MEA-GL mixtures are also observed (Fig. 3c). Beyond that, four

208   extra IML compounds are also observed at m/z values of 113.071, 141.066, 159.076 and 171.076, corresponding to IML

209   (IML$_{MAG}$), imidazole-2-carboxaldehyde (IC$_{MAG}$) and its hydrated form (HIC$_{MAG}$), and N-glyoxal substituted imidazole (GI$_{MAG}$)

210   (Figs. 3c and S12). An extra -C$_2$H$_4$O group exists in the geometries of the above four IML compounds relative to the products

211   of AL-GL mixture, indicating that there exist the cross reactions between MEA and AS in the MEA-AS-GL mixture. As shown

212   in Fig. 5, the cross NA reaction between ID$_{AS}$ and MEA or ID$_{MEA}$ and AS possesses a negative ΔG_r value of -4.8 or -5.4 kcal

213   mol^{-1}, followed by dehydration to form the same intermediate, diimine (DI$_{MAG}$). It implies that the cross reactions in MEA-

214   AS-GL mixture are thermodynamical favorable. Therefore, the formation and propagation of chromophores in MEA-AS-GL

215   mixture also proceed via NA reactions, which is the key route for the formation of BrC chromophores.

216   As shown in Fig. 3c, no bicyclic IML compounds are produced in MEA-AS-GL mixture because the precursors of bicyclic

217   IML compound (i.e., imidazole-2-carboxaldehyde) is fully hydrated under more acidic condition than AS-GL mixture (see pH

218   values in Table S2). It leads to the formation of N-glyoxal substituted imidazole (i.e., GI$_{MAG}$) instead of bicyclic IML

219   compounds. The similar phenomenon is also found in the previous studies (Ackendorf et al., 2017; Kampf et al., 2012; Yu et

220   al., 2011) that bicyclic IML compounds are hardly yield from imidazole-2-carboxaldehyde in acidic condition. As discussed

221   above, imidazole-based structural characteristics in chromophores are maintained in the presence of MEA, but the

222   nucleophilicity of chromophores is reduced because the nucleophilic sites are occupied. Also, the positively charged quaternary

223   amine salts (such as IC$_{MEA}$ and GI$_{MAG}$) are also yield in MEA-GL and MEA-AS-GL mixtures, and thereby the chemical

224   composition and optical properties of chromophores are affected.

225   **3.3 Chemical reaction mechanism leading to BrC chromophores**

226   As discussed above, the four-step NA reactions are the key pathways to form and propagate oligomers including intermediates

227   and chromophores for three mixtures. Therefore, all possible pathways involved in the four key NA reactions of three mixtures

are calculated using density functional theory. The corresponding PESs stablished by the M06-2X/6-311+G(3df,3pd)//M06-2X/6-311G(d,p) level are also presented in dotted boxes of Figs. 4-5. The optimized geometries of key stationary points, including transition states (TSs), intermediates, and products, are depicted in Figs. S13-S15 at the M06-2X/6-311G(d,p) level. We first performed quantum chemistry calculation to evaluated the direct nucleophilic attack of GL by MEA or AS, which proceeds a large activation energy ($\Delta G^{\ddagger}$) value of 6.3 or 8.6 kcal mol^{-1}, following by H-shift reaction to yield AHA$_{MEA}$ or AHA$_{AS}$, with also a large $\Delta G^{\ddagger}$ value of 15.2 or 18.2 kcal mol^{-1} (see NA1a' and NA2a' in Fig. 4). The high $\Delta G^{\ddagger}$ values and large endothermicity of the direct NA reactions leading to AHA$_{MEA}$ and AHA$_{AS}$ imply that their occurrences are kinetically and thermodynamically hindered.

Hence, we explored the cationic oligomerization of chromophore formation under acidic condition, which involves three essential steps, (1) protonation and dehydration to form cationic intermediates (CIs) or carbenium ions (CBs), (2) nucleophilic attack of CIs or CBs by MEA and AS, and (3) formation of intermediates and chromophores by deprotonation or dehydration. As shown in Figs. 4-5, each pathway involved in the cationic-mediated reaction mechanism proceeds without a TS, except deprotonation of CIs, in line with the results of the previous studies (Ji et al., 2020; Ji et al., 2022). However, deprotonation of CIs by sulfate ion (SO$_4^{2-}$) possesses a negative $\Delta G^{\ddagger}$ value in this study, implying an approximate barrierless process of this kind of deprotonation.

For the first-step NA reaction (NA1a in Fig. 4) in MEA-GL mixture, the electrophilic cationic site of CB$_{DL}$ is attacked by the nucleophilic -NH$_2$ group of MEA with the ΔG_r value of -40.3 kcal mol^{-1}. CB$_{DL}$ is broadly produced from GL and reflected from the large particle growth and formation of IML products (Ji et al., 2020; Li et al., 2021). The deprotonation of CI$_{MEA}$1 possesses a negative $\Delta G^{\ddagger}$ value of -4.5 kcal mol^{-1}, and a pre-reactive complex is identified prior the corresponding TS (detailed in SI). Similarly, the other two NA1b and NA1c reactions (Fig. 4) also include protonation, dehydration, nucleophilic attack, and deprotonation to yield HA$_{MEA}$ and PIC $_{MEA}$. Kinetic data listed in Table S3 show that the rate constants of most pathways involved in the NA1a-1b and NA2a-2c reactions fall in the range of ~10^9 M^{-1} s^{-1}. The similar results can be drawn for AS-GL mixture, suggesting that the electrostatic attraction is a significant factor to affect the NA reactions.

To further evaluate the cationic reaction mechanism, the natural bond orbital (NBO) analysis reveals that the N atom of NH$_3$ exhibits more negative charge (-1.1 e) relative to MEA (-0.9 e), suggesting the stronger electrostatic attraction between CB$_{DL}$ and NH$_3$ to yield CI$_{AS}$1 in the first-step NA reaction (see NA1a and NA2a in Fig. 4). However, the second-step NA reaction between CB$_{MEA}$ and MEA are promoted by MEA because the presence of MEA enhances the positive charge in CB$_{MEA}$ (0.6 e), facilitating the electrostatic attraction (see NA1b and NA2b in Fig. 4). For the third-step NA reaction (see NA1c and NA2c in Fig. 4), due to the steric hindrance, the deprotonation of CI$_{MEA}$8 possesses a larger $\Delta G^{\ddagger}$ value relative to that of CI$_{AS}$8. Hence, the NA reactions are regulated by both electrostatic attraction and steric hindrance effect.

The fourth-step NA reactions in MEA-GL and AS-GL mixtures exhibit two distinct chemical reaction mechanisms in cyclization to yield N-heterocycles (see NA1d and NA2d in Fig. 4). The protonation of PIC$_{MEA}$ and PIC$_{AS}$ occurs at the hydroxyl group to form CI$_{MEA}$9 and CI$_{AS}$9. For MEA-GL mixture, the barrierless dehydration and cyclization of CI$_{MEA}$9 occur in one step to yield N-heterocycle (i.e., IC$_{MEA}$), with the total ΔG_r value of -78.6 kcal mol^{-1} (NA1d in Fig. 4a). However, for

AS-GL mixture, the cyclization of PIC$_{AS}$ to IC$_{AS}$ includes protonation, dehydration, cyclization, and deprotonation. Note that cyclization and deprotonation proceed via two TSs in sequence, with the corresponding $\Delta G^{\ddagger}$ values of 3.9 and -0.6 kcal mol^{-1} (NA2d in Fig. 4b), respectively, forming IC$_{AS}$. As discussed above, cyclization in MEA-GL and AS-GL mixtures is the rate-limiting step to chromophore formation.

For MEA-AS-GL mixture, AHA$_{MEA/AS}$, and ID$_{MEA/AS}$ are yielded via the same first NA reactions (NA1a/2a) as MEA-GL and AS-GL mixtures. Also, the formation of ID$_{MEA/AS}$ proceeds via protonation and dehydration to form CB$_{MEA/AS}$. However, the second NA reaction includes the cross-NA reaction of CB$_{MEA}$ with AS (NA3b-1) or CB$_{AS}$ with MEA (NA3b-2) to produce extra oligomers (i.e., HA$_{MAG}$1 and HA$_{MAG}$2), in contrast to MEA-GL and AS-GL mixtures. Hence, the fate of CB$_{MEA/AS}$ is dependent of the competition reaction between the pathways of self-NA reaction to form HA$_{MEA/AS}$ (NA1b/2b) and cross-NA reaction to yield HA$_{MAG}$1/2 (NA3b-1/2). The ΔG_r values of the cross-NA reactions to yield HA$_{MAG}$1 and HA$_{MAG}$2 are -30.3 and -30.4 kcal mol^{-1}, respectively, comparable with those of self-NA reactions. It suggests both NA reactions to form HAs are equally accessible. Subsequently, HA$_{MAG}$1/2 undergoes dehydration to form DI$_{MAG}$, further proceeds the third NA reaction to yield PIC$_{MAG}$, in line with the mechanisms of the third NA reactions for MEA-GL and AS-GL mixtures. The cyclization of CI$_{MAG}$10 (the fourth NA reaction) possesses with two successive TSs, similar to that of AS-GL mixture but different to that of MEA-GL mixture. The corresponding $\Delta G^{\ddagger}$ values are obtained as 5.0 and 1.6 kcal mol^{-1}, respectively, which are larger than those of AS-GL mixture. In summary, compared with the AS-containing mixtures, the presence of MEA provides the extra two branched chains in N atoms, which affect the natural charges and molecular steric hindrance of intermediates, to thereby facilitate the intramolecular interaction between N and C atoms to form SBrC chromophores.

4 Conclusions and atmospheric implications

BrC chromophores play an important role in the Earth's radiative balance, air quality and human health. However, the formation mechanisms of BrC chromophores are not fully understood, hindering a comprehensive assessment of BrC chromophores on atmospheric chemistry and environmental impacts. Hence, using combined theoretical and experimental methods, we investigated the aqueous chemistry of typical RNCs with GL and evaluated the impact of typical multifunctional RNCs on the formation of BrC chromophores. Experimental studies show that the MAC values of chromophores are affected by the initial pH value for AS-GL, MEA-GL and MEA-AS-GL mixtures, and the growth rates of chromophores are enhanced in the presence of MEA. The optical properties of chromophores are regulated by monocyclic and bicyclic IML compounds in AS-GL mixture but by monocyclic IML compounds in MEA-containing mixtures (i.e., MEA-GL and MEA-AS-GL). Combined with the results of quantum chemical calculations, chromophore formation is characterized by nucleophilic addition with large exothermicity and strong electrostatic attraction among the MEA-derived intermediates, which are also enhanced by MEA.

In addition, to simply evaluate the impacts of MEA and AS on chromosphere formation in the aqueous aerosols and fog/cloud droplets, the dynamics process of GL from gas to aqueous phase was carried out (Fig. S16). The free energy

difference reflects whether the liquid particles with MEA and AS (denoted as MEA and AS particles) prefer to adsorb and accommodate GL. As shown in Fig. S16, a larger decrease in the free energy (-3.7 kcal mol^{-1}) occurs when GL approaches the interface of the MEA particle relative to the AS particle, indicating a thermodynamically favorable process. Subsequently, the stabilized GL enters into the interior region of the MEA and AS particles, with slightly endothermic (1.6 and 2.4 kcal mol^{-1}). A smaller free energy difference from the interface into the interior region of the MEA particle implies that the interfacial GL is more readily promoted to enter the interior region of the particle when the particles contain MEA compared with AS. Hence, the interfacial and interior attraction on the MEA particle is more pronounced for small α-dicarbonyls, to facilitate the further engagement in the aqueous-phase reactions with RNCs in the particle.

Formation of SBrC from multifunctional RNCs and small α-dicarbonyls occurs widely on aqueous aerosols and fog/cloud droplets under typical atmospheric conditions. Compared with the ubiquitous coexistence between AS and small α-dicarbonyls from global aerosol measurement, SBrC aerosol formation from multifunctional RNC mixtures should be paid attention to during serious haze formation in China because of their atmospheric reactivities and non-negligible concentrations. Our results also imply that SBrC aerosols, if formed from the aqueous reactions between MEA and GL, likely contribute to atmospheric warming because the presence of MEA enhances the MACs of the mixture. Hence, recognition of this aerosol formation mechanism in the radiative transfer atmospheric model is needed, reparenting a possible missing source for BrC formation on urban, regional and global scales.

Review statement. This paper was edited and reviewed by two anonymous referees.

References

Ackendorf, J. M., Ippolito, M. G., and Galloway, M. M.: pH Dependence of the Imidazole-2-carboxaldehyde Hydration Equilibrium: Implications for Atmospheric Light Absorbance, Environ. Sci. Technol. Lett., 4, 551-555, https://doi.org/10.1021/acs.estlett.7b00486, 2017.

Aiona, P. K., Lee, H. J., Leslie, R., Lin, P., Laskin, A., Laskin, J., and Nizkorodov, S. A.: Photochemistry of Products of the Aqueous Reaction of Methylglyoxal with Ammonium Sulfate, ACS Earth Space Chem., 1, 522-532, https://doi.org/10.1021/acsearthspacechem.7b00075, 2017.

An, Z., Huang, R. J., Zhang, R., Tie, X., Li, G., Cao, J., Zhou, W., Shi, Z., Han, Y., Gu, Z., and Ji, Y.: Severe haze in northern China: A synergy of anthropogenic emissions and atmospheric processes, Proc. Natl. Acad. Sci. U. S. A., 116, 8657-8666, https://doi.org/10.1073/pnas.1900125116, 2019.

Chen, Y. and Bond, T. C.: Light absorption by organic carbon from wood combustion, Atmos. Chem. Phys., 10, 1773-1787, https://doi.org/DOI 10.5194/acp-10-1773-2010, 2010.

Collins, F. C. and Kimball, G. E.: Diffusion-controlled reaction rates, J. Colloid Sci., 4, 425-437, https://doi.org/https://doi.org/10.1016/0095-8522(49)90023-9, 1949.

Corbin, J. C., Czech, H., Massabò, D., de Mongeot, F. B., Jakobi, G., Liu, F., Lobo, P., Mennucci, C., Mensah, A. A., Orasche, J., Pieber, S. M., Prévôt, A. S. H., Stengel, B., Tay, L. L., Zanatta, M., Zimmermann, R., El Haddad, I., and Gysel, M.: Infrared-absorbing carbonaceous tar can dominate light absorption by marine-engine exhaust, npj Clim. Atmos. Sci., 2, https://doi.org/10.1038/s41612-019-0069-5, 2019.

De Haan, D. O., Tolbert, M. A., and Jimenez, J. L.: Atmospheric condensed-phase reactions of glyoxal with methylamine, Geophys. Res. Lett., 36, https://doi.org/10.1029/2009gl037441, 2009a.

De Haan, D. O., Corrigan, A. L., Smith, K. W., Stroik, D. R., Turley, J. J., Lee, F. E., Tolbert, M. A., Jimenez, J. L., Cordova, K. E., and Ferrell, G. R.: Secondary Organic Aerosol-Forming Reactions of Glyoxal with Amino Acids, Environ. Sci. Technol., 43, 2818-2824, https://doi.org/10.1021/es803534f, 2009b.

De Haan, D. O., Hawkins, L. N., Jansen, K., Welsh, H. G., Pednekar, R., de Loera, A., Jimenez, N. G., Tolbert, M. A., Cazaunau, M., Gratien, A., Bergé, A., Pangui, E., Formenti, P., and Doussin, J.-F.: Glyoxal's impact on dry ammonium salts: fast and reversible surface aerosol browning, Atmos. Chem. Phys., 20, 9581-9590, https://doi.org/10.5194/acp-20-9581-2020, 2020.

De Haan, D. O., Tapavicza, E., Riva, M., Cui, T., Surratt, J. D., Smith, A. C., Jordan, M. C., Nilakantan, S., Almodovar, M., Stewart, T. N., de Loera, A., De Haan, A. C., Cazaunau, M., Gratien, A., Pangui, E., and Doussin, J. F.: Nitrogen-Containing, Light-Absorbing Oligomers Produced in Aerosol Particles Exposed to Methylglyoxal, Photolysis, and Cloud Cycling, Environ.

352 Sci. Technol., 52, 4061-4071, https://doi.org/10.1021/acs.est.7b06105, 2018.

353 De Haan, D. O., Pajunoja, A., Hawkins, L. N., Welsh, H. G., Jimenez, N. G., De Loera, A., Zauscher, M., Andretta, A. D.,

354 Joyce, B. W., De Haan, A. C., Riva, M., Cui, T., Surratt, J. D., Cazaunau, M., Formenti, P., Gratien, A., Pangui, E., and Doussin,

355 J.-F.: Methylamine's Effects on Methylglyoxal-Containing Aerosol: Chemical, Physical, and Optical Changes, ACS Earth

356 Space Chem., 3, 1706-1716, https://doi.org/10.1021/acsearthspacechem.9b00103, 2019.

357 Evans, M. G. and Polanyi, M.: Some applications of the transition state method to the calculation of reaction velocities,

358 especially in solution, Trans. Faraday Soc., 31, 875-894, https://doi.org/10.1039/TF9353100875, 1935.

359 Eyring, H.: The Activated Complex in Chemical Reactions, J. Chem. Phys., 3, 107-115, https://doi.org/10.1063/1.1749604,

360 1935.

361 Fu, T.-M., Jacob, D. J., Wittrock, F., Burrows, J. P., Vrekoussis, M., and Henze, D. K.: Global budgets of atmospheric glyoxal

362 and methylglyoxal, and implications for formation of secondary organic aerosols, J. Geophys. Res., 113,

363 https://doi.org/10.1029/2007jd009505, 2008.

364 Galano, A. and Alvarez-Idaboy, J. R.: Guanosine + OH Radical Reaction in Aqueous Solution: A Reinterpretation of the

365 UV−vis Data Based on Thermodynamic and Kinetic Calculations, Org. Lett., 11, 5114-5117,

366 https://doi.org/10.1021/ol901862h, 2009.

367 Galloway, M. M., Chhabra, P. S., Chan, A. W. H., Surratt, J. D., Flagan, R. C., Seinfeld, J. H., and Keutsch, F. N.: Glyoxal

368 uptake on ammonium sulphate seed aerosol: reaction products and reversibility of uptake under dark and irradiated conditions,

369 Atmos. Chem. Phys., 9, 3331-3345, https://doi.org/10.5194/acp-9-3331-2009, 2009.

370 Gao, Y., Ji, Y., Li, G., and An, T.: Mechanism, kinetics and toxicity assessment of OH-initiated transformation of triclosan in

371 aquatic environments, Water Res., 49, 360-370, https://doi.org/10.1016/j.watres.2013.10.027, 2014.

372 Gao, Y., Ji, Y., Li, G., Mai, B., and An, T.: Bioaccumulation and ecotoxicity increase during indirect photochemical

373 transformation of polycyclic musk tonalide: A modeling study, Water Res., 105, 47-55,

374 https://doi.org/10.1016/j.watres.2016.08.055, 2016.

375 Ge, X., Wexler, A. S., and Clegg, S. L.: Atmospheric amines – Part I. A review, Atmos. Environ., 45, 524-546,

376 https://doi.org/10.1016/j.atmosenv.2010.10.012, 2011.

377 George, C., Ammann, M., D'Anna, B., Donaldson, D. J., and Nizkorodov, S. A.: Heterogeneous photochemistry in the

378 atmosphere, Chem. Rev., 115, 4218-4258, https://doi.org/10.1021/cr500648z, 2015.

379 Gomez, M. E., Lin, Y., Guo, S., and Zhang, R.: Heterogeneous Chemistry of Glyoxal on Acidic Solutions. An Oligomerization

380 Pathway for Secondary Organic Aerosol Formation, The J. Phys. Chem. A, 119, 4457-4463, https://doi.org/10.1021/jp509916r,

381 2015.

382 Hamilton, J. F., Baeza-Romero, M. T., Finessi, E., Rickard, A. R., Healy, R. M., Peppe, S., Adams, T. J., Daniels, M. J. S., Ball,

383 S. M., Goodall, I. C. A., Monks, P. S., Borrás, E., and Muñoz, A.: Online and offline mass spectrometric study of the impact

384 of oxidation and ageing on glyoxal chemistry and uptake onto ammonium sulfate aerosols, Faraday Discuss., 165,

385 https://doi.org/10.1039/c3fd00051f, 2013.

Hawkins, L. N., Welsh, H. G., and Alexander, M. V.: Evidence for pyrazine-based chromophores in cloud water mimics containing methylglyoxal and ammonium sulfate, Atmos. Chem. Phys., 18, 12413-12431, https://doi.org/10.5194/acp-18-12413-2018, 2018.

Huang, X., Deng, C., Zhuang, G., Lin, J., and Xiao, M.: Quantitative analysis of aliphatic amines in urban aerosols based on online derivatization and high performance liquid chromatography, Environ. Sci.: Processes Impacts, 18, 796-801, https://doi.org/10.1039/c6em00197a, 2016.

Ji, Y., Shi, Q., Ma, X., Gao, L., Wang, J., Li, Y., Gao, Y., Li, G., Zhang, R., and An, T.: Elucidating the critical oligomeric steps in secondary organic aerosol and brown carbon formation, Atmos. Chem. Phys., 22, 7259-7271, https://doi.org/10.5194/acp-22-7259-2022, 2022.

Ji, Y., Shi, Q., Li, Y., An, T., Zheng, J., Peng, J., Gao, Y., Chen, J., Li, G., Wang, Y., Zhang, F., Zhang, A. L., Zhao, J., Molina, M. J., and Zhang, R.: Carbenium ion-mediated oligomerization of methylglyoxal for secondary organic aerosol formation, Proc. Natl. Acad. Sci. U. S. A., 117, 13294-13299, https://doi.org/10.1073/pnas.1912235117, 2020.

Ji, Y., Zhao, J., Terazono, H., Misawa, K., Levitt, N. P., Li, Y., Lin, Y., Peng, J., Wang, Y., Duan, L., Pan, B., Zhang, F., Feng, X., An, T., Marrero-Ortiz, W., Secrest, J., Zhang, A. L., Shibuya, K., Molina, M. J., and Zhang, R.: Reassessing the atmospheric oxidation mechanism of toluene, Proc. Natl. Acad. Sci. U. S. A., 114, 8169, https://doi.org/10.1073/pnas.1705463114, 2017.

Jorgensen, W. L., Maxwell, D. S., and Tirado-Rives, J.: Development and Testing of the OPLS All-Atom Force Field on Conformational Energetics and Properties of Organic Liquids, J. Am. Chem. Soc., 118, 11225-11236, https://doi.org/10.1021/ja9621760, 1996.

Kampf, C. J., Jakob, R., and Hoffmann, T.: Identification and characterization of aging products in the glyoxal/ammonium sulfate system – implications for light-absorbing material in atmospheric aerosols, Atmos. Chem. Phys., 12, 6323-6333, https://doi.org/10.5194/acp-12-6323-2012, 2012.

Kampf, C. J., Filippi, A., Zuth, C., Hoffmann, T., and Opatz, T.: Secondary brown carbon formation via the dicarbonyl imine pathway: nitrogen heterocycle formation and synergistic effects, Phys. Chem. Chem. Phys., 18, 18353-18364, https://doi.org/10.1039/c6cp03029g, 2016.

Karl, M., Wright, R. F., Berglen, T. F., and Denby, B.: Worst case scenario study to assess the environmental impact of amine emissions from a CO_2 capture plant, Int. J. Greenh. Gas Control, 5, 439-447, https://doi.org/10.1016/j.ijggc.2010.11.001, 2011.

Kasthuriarachchi, N. Y., Rivellini, L. H., Adam, M. G., and Lee, A. K. Y.: Light Absorbing Properties of Primary and Secondary Brown Carbon in a Tropical Urban Environment, Environ. Sci. Technol., 54, 10808-10819, https://doi.org/10.1021/acs.est.0c02414, 2020.

Kumar, S., Rosenberg, J. M., Bouzida, D., Swendsen, R. H., and Kollman, P. A.: The weighted histogram analysis method for free-energy calculations on biomolecules. I. The method, J. Comput. Chem., 13, 1011-1021, https://doi.org/10.1002/jcc.540130812, 1992.

Laskin, A., Laskin, J., and Nizkorodov, S. A.: Chemistry of atmospheric brown carbon, Chem. Rev., 115, 4335-4382, https://doi.org/10.1021/cr5006167, 2015.

Lee, A. K. Y., Zhao, R., Li, R., Liggio, J., Li, S.-M., and Abbatt, J. P. D.: Formation of Light Absorbing Organo-Nitrogen Species from Evaporation of Droplets Containing Glyoxal and Ammonium Sulfate, Environ. Sci. Technol., 47, 12819-12826, https://doi.org/10.1021/es402687w, 2013.

Lee, H. J., Aiona, P. K., Laskin, A., Laskin, J., and Nizkorodov, S. A.: Effect of solar radiation on the optical properties and molecular composition of laboratory proxies of atmospheric brown carbon, Environ. Sci. Technol., 48, 10217-10226, https://doi.org/10.1021/es502515r, 2014.

Leontyev, I. and Stuchebrukhov, A.: Accounting for electronic polarization in non-polarizable force fields, Phys. Chem. Chem. Phys., 13, 2613-2626, https://doi.org/10.1039/c0cp01971b, 2011.

Li, X., Sun, N., Jin, Q., Zhao, Z., Wang, L., Wang, Q., Gu, X., Li, Y., and Liu, X.: Light absorption properties of black and brown carbon in winter over the North China Plain: Impacts of regional biomass burning, Atmos. Environ., 278, https://doi.org/10.1016/j.atmosenv.2022.119100, 2022.

Li, Y., Ji, Y., Zhao, J., Wang, Y., Shi, Q., Peng, J., Wang, Y., Wang, C., Zhang, F., Wang, Y., Seinfeld, J. H., and Zhang, R.: Unexpected Oligomerization of Small alpha-Dicarbonyls for Secondary Organic Aerosol and Brown Carbon Formation, Environ. Sci. Technol., 55, 4430-4439, https://doi.org/10.1021/acs.est.0c08066, 2021.

Lin, P., Laskin, J., Nizkorodov, S. A., and Laskin, A.: Revealing Brown Carbon Chromophores Produced in Reactions of Methylglyoxal with Ammonium Sulfate, Environ. Sci. Technol., 49, 14257-14266, https://doi.org/10.1021/acs.est.5b03608, 2015.

Liu, D., He, C., Schwarz, J. P., and Wang, X.: Lifecycle of light-absorbing carbonaceous aerosols in the atmosphere, npj Clim. Atmos. Sci., 3, 40, https://doi.org/10.1038/s41612-020-00145-8, 2020.

M. J.Frisch, G. W. T., H. B.Schlegel, G. E.Scuseria, M. A.Robb, J. R.Cheeseman, G.Scalmani, V.Barone, B.Mennucci, G. A.Petersson, H.Nakatsuji, M.Caricato, X.Li, H. P.Hratchian, A. F.Izmaylov, J.Bloino, G.Zheng, J. L.Sonnenberg, M.Hada, M.Ehara, K.Toyota, R.Fukuda, J.Hasegawa, M.Ishida, T.Nakajima, Y.Honda, O.Kitao, H.Nakai, T.Vreven, J. A.Montgomery, Jr., J. E.Peralta, F.Ogliaro, M.Bearpark, J. J.Heyd, E.Brothers, K. N.Kudin, V. N.Staroverov, T.Keith, R.Kobayashi, J.Normand, K.Raghavachari, A.Rendell, J. C.Burant, S. S.Iyengar, J.Tomasi, M.Cossi, N.Rega, J. M.Millam, M.Klene, J. E.Knox, J. B.Cross, V.Bakken, C.Adamo, J.Jaramillo, R.Gomperts, R. E.Stratmann, O.Yazyev, A. J.Austin, R.Cammi, C.Pomelli, J. W.Ochterski, R. L.Martin, K.Morokuma, V. G.Zakrzewski, G. A.Voth, P.Salvador, J. J.Dannenberg, S.Dapprich, A. D.Daniels, O.Farkas, J. B.Foresman, J. V.Ortiz, J.Cioslowski and D. J.Fox: Gaussian 09, Revision D.01, Gaussian, Inc., Wallingford CT, 2013, 2013.

Marenich, A. V., Cramer, C. J., and Truhlar, D. G.: Universal Solvation Model Based on Solute Electron Density and on a Continuum Model of the Solvent Defined by the Bulk Dielectric Constant and Atomic Surface Tensions, J. Phys. Chem. B, 113, 6378-6396, https://doi.org/10.1021/jp810292n, 2009.

Marrero-Ortiz, W., Hu, M., Du, Z., Ji, Y., Wang, Y., Guo, S., Lin, Y., Gomez-Hernandez, M., Peng, J., Li, Y., Secrest, J., Zamora, M. L., Wang, Y., An, T., and Zhang, R.: Formation and Optical Properties of Brown Carbon from Small α-Dicarbonyls and Amines, Environ. Sci. Technol., 53, 117-126, https://doi.org/10.1021/acs.est.8b03995, 2018.

Martins-Costa, M. T., Anglada, J. M., Francisco, J. S., and Ruiz-Lopez, M. F.: Reactivity of volatile organic compounds at the surface of a water droplet, J. Am. Chem. Soc., 134, 11821-11827, https://doi.org/10.1021/ja304971e, 2012.

Moise, T., Flores, J. M., and Rudich, Y.: Optical properties of secondary organic aerosols and their changes by chemical processes, Chem. Rev., 115, 4400-4439, https://doi.org/10.1021/cr5005259, 2015.

Mosallanejad, S., Oluwoye, I., Altarawneh, M., Gore, J., and Dlugogorski, B. Z.: Interfacial and bulk properties of concentrated solutions of ammonium nitrate, Phys. Chem. Chem. Phys., 22, 27698-27712, https://doi.org/10.1039/d0cp04874g, 2020.

Myriokefalitakis, S., Vrekoussis, M., Tsigaridis, K., Wittrock, F., Richter, A., Brühl, C., Volkamer, R., Burrows, J. P., and Kanakidou, M.: The influence of natural and anthropogenic secondary sources on the glyoxal global distribution, Atmos. Chem. Phys., 8, 4965-4981, https://doi.org/10.5194/acp-8-4965-2008, 2008.

Nie, W., Yan, C., Huang, D. D., Wang, Z., Liu, Y., Qiao, X., Guo, Y., Tian, L., Zheng, P., Xu, Z., Li, Y., Xu, Z., Qi, X., Sun, P., Wang, J., Zheng, F., Li, X., Yin, R., Dallenbach, K. R., Bianchi, F., Petäjä, T., Zhang, Y., Wang, M., Schervish, M., Wang, S., Qiao, L., Wang, Q., Zhou, M., Wang, H., Yu, C., Yao, D., Guo, H., Ye, P., Lee, S., Li, Y. J., Liu, Y., Chi, X., Kerminen, V.-M., Ehn, M., Donahue, N. M., Wang, T., Huang, C., Kulmala, M., Worsnop, D., Jiang, J., and Ding, A.: Secondary organic aerosol formed by condensing anthropogenic vapours over China's megacities, Nat. Geosci., 15, 255-261, https://doi.org/10.1038/s41561-022-00922-5, 2022.

Ning, A., Liu, L., Zhang, S., Yu, F., Du, L., Ge, M., and Zhang, X.: The critical role of dimethylamine in the rapid formation of iodic acid particles in marine areas, npj Clim. Atmos. Sci., 5, 92, https://doi.org/10.1038/s41612-022-00316-9, 2022.

Nozière, B., Dziedzic, P., and Córdova, A.: Products and Kinetics of the Liquid-Phase Reaction of Glyoxal Catalyzed by Ammonium Ions ($NH4^+$), J. Phys. Chem. A, 113, 231-237, https://doi.org/10.1021/jp8078293, 2009.

Okuno, Y.: Theoretical Investigation of the Mechanism of the Baeyer-Villiger Reaction in Nonpolar Solvents, Chem. - Eur. J., 3, 212-218, https://doi.org/https://doi.org/10.1002/chem.19970030208, 1997.

Phillips, J. C., Braun, R., Wang, W., Gumbart, J., Tajkhorshid, E., Villa, E., Chipot, C., Skeel, R. D., Kale, L., and Schulten, K.: Scalable molecular dynamics with NAMD, J. Comput. Chem., 26, 1781-1802, https://doi.org/10.1002/jcc.20289, 2005.

Powelson, M. H., Espelien, B. M., Hawkins, L. N., Galloway, M. M., and De Haan, D. O.: Brown Carbon Formation by Aqueous-Phase Carbonyl Compound Reactions with Amines and Ammonium Sulfate, Environ. Sci. Technol., 48, 985-993, https://doi.org/10.1021/es4038325, 2014a.

Powelson, M. H., Espelien, B. M., Hawkins, L. N., Galloway, M. M., and De Haan, D. O.: Brown carbon formation by aqueous-phase carbonyl compound reactions with amines and ammonium sulfate, Environ. Sci. Technol., 48, 985-993, https://doi.org/10.1021/es4038325, 2014b.

Puxty, G., Rowland, R., Allport, A., Yang, Q., Bown, M., Burns, R., Maeder, M., and Attalla, M.: Carbon Dioxide Postcombustion Capture: A Novel Screening Study of the Carbon Dioxide Absorption Performance of 76 Amines, Environ. Sci. Technol., 43, 6427-6433, https://doi.org/10.1021/es901376a, 2009.

Sedehi, N., Takano, H., Blasic, V. A., Sullivan, K. A., and De Haan, D. O.: Temperature- and pH-dependent aqueous-phase kinetics of the reactions of glyoxal and methylglyoxal with atmospheric amines and ammonium sulfate, Atmos. Environ., 77,

656-663, https://doi.org/10.1016/j.atmosenv.2013.05.070, 2013.

Shen, J., Xie, H.-B., Elm, J., Ma, F., Chen, J., and Vehkamäki, H.: Methanesulfonic Acid-driven New Particle Formation Enhanced by Monoethanolamine: A Computational Study, Environ. Sci. Technol., 53, 14387-14397, https://doi.org/10.1021/acs.est.9b05306, 2019.

Shi, Q., Zhang, W., Ji, Y., Wang, J., Qin, D., Chen, J., Gao, Y., Li, G., and An, T.: Enhanced uptake of glyoxal at the acidic nanoparticle interface: implications for secondary organic aerosol formation, Environ. Sci.: Nano, 7, 1126-1135, https://doi.org/10.1039/d0en00016g, 2020.

Srivastava, D., Vu, T. V., Tong, S., Shi, Z., and Harrison, R. M.: Formation of secondary organic aerosols from anthropogenic precursors in laboratory studies, npj Clim. Atmos. Sci., 5, https://doi.org/10.1038/s41612-022-00238-6, 2022.

Torrie, G. M. and Valleau, J. P.: Nonphysical sampling distributions in Monte Carlo free-energy estimation: Umbrella sampling, J. Comput. Phys., 23, 187-199, https://doi.org/https://doi.org/10.1016/0021-9991(77)90121-8, 1977.

Trainic, M., Riziq, A. A., Lavi, A., and Rudich, Y.: Role of interfacial water in the heterogeneous uptake of glyoxal by mixed glycine and ammonium sulfate aerosols, J. Phys. Chem. A, 116, 5948-5957, https://doi.org/10.1021/jp2104837, 2012.

Tuccella, P., Curci, G., Pitari, G., Lee, S., and Jo, D. S.: Direct Radiative Effect of Absorbing Aerosols: Sensitivity to Mixing State, Brown Carbon, and Soil Dust Refractive Index and Shape, J. Geophys. Res.: Atmos., 125, https://doi.org/10.1029/2019jd030967, 2020.

Wang, X., Heald, C. L., Liu, J., Weber, R. J., Campuzano-Jost, P., Jimenez, J. L., Schwarz, J. P., and Perring, A. E.: Exploring the observational constraints on the simulation of brown carbon, Atmos. Chem. Phys., 18, 635-653, https://doi.org/10.5194/acp-18-635-2018, 2018.

Wang, X., Hayeck, N., Brüggemann, M., Yao, L., Chen, H., Zhang, C., Emmelin, C., Chen, J., George, C., and Wang, L.: Chemical Characteristics of Organic Aerosols in Shanghai: A Study by Ultrahigh-Performance Liquid Chromatography Coupled With Orbitrap Mass Spectrometry, J. Geophys. Res.: Atmos., 122, 11,703-711,722, https://doi.org/10.1002/2017jd026930, 2017.

Yan, J., Wang, X., Gong, P., Wang, C., and Cong, Z.: Review of brown carbon aerosols: Recent progress and perspectives, Sci. Total Environ., 634, 1475-1485, https://doi.org/10.1016/j.scitotenv.2018.04.083, 2018.

Yang, Z., Tsona, N. T., George, C., and Du, L.: Nitrogen-Containing Compounds Enhance Light Absorption of Aromatic-Derived Brown Carbon, Environ. Sci. Technol., 56, 4005-4016, https://doi.org/10.1021/acs.est.1c08794, 2022.

Yu, G., Bayer, A. R., Galloway, M. M., Korshavn, K. J., Fry, C. G., and Keutsch, F. N.: Glyoxal in aqueous ammonium sulfate solutions: products, kinetics and hydration effects, Environ. Sci. Technol., 45, 6336-6342, https://doi.org/10.1021/es200989n, 2011.

Yuan, W., Huang, R.-J., Shen, J., Wang, K., Yang, L., Wang, T., Gong, Y., Cao, W., Guo, J., Ni, H., Duan, J., and Hoffmann, T.: More water-soluble brown carbon after the residential "coal-to-gas" conversion measure in urban Beijing, npj Clim. Atmos. Sci., 6, https://doi.org/10.1038/s41612-023-00355-w, 2023.

Yuan, W., Huang, R.-J., Yang, L., Guo, J., Chen, Z., Duan, J., Wang, T., Ni, H., Han, Y., Li, Y., Chen, Q., Chen, Y., Hoffmann,

T., and O'Dowd, C.: Characterization of the light-absorbing properties, chromophore composition and sources of brown carbon aerosol in Xi'an, northwestern China, Atmos. Chem. Phys., 20, 5129-5144, https://doi.org/10.5194/acp-20-5129-2020, 2020.

Zhang, A., Wang, Y., Zhang, Y., Weber, R. J., Song, Y., Ke, Z., and Zou, Y.: Modeling the global radiative effect of brown carbon: a potentially larger heating source in the tropical free troposphere than black carbon, Atmos. Chem. Phys., 20, 1901-1920, https://doi.org/10.5194/acp-20-1901-2020, 2020.

Zhang, W., Ji, Y., Li, G., Shi, Q., and An, T.: The heterogeneous reaction of dimethylamine/ammonia with sulfuric acid to promote the growth of atmospheric nanoparticles, Environ. Sci.: Nano, 6, 2767-2776, https://doi.org/10.1039/c9en00619b, 2019.

Zhang, X., Tong, S., Jia, C., Zhang, W., Wang, Z., Tang, G., Hu, B., Liu, Z., Wang, L., Zhao, P., Pan, Y., and Ge, M.: Elucidating HONO formation mechanism and its essential contribution to OH during haze events, npj Clim. Atmos. Sci., 6, 55, https://doi.org/10.1038/s41612-023-00371-w, 2023.

Zhao, R., Lee, A. K. Y., Huang, L., Li, X., Yang, F., and Abbatt, J. P. D.: Photochemical processing of aqueous atmospheric brown carbon, Atmos. Chem. Phys., 15, 6087-6100, https://doi.org/10.5194/acp-15-6087-2015, 2015.

Zhao, Y. and Truhlar, D. G.: The M06 suite of density functionals for main group thermochemistry, thermochemical kinetics, noncovalent interactions, excited states, and transition elements: two new functionals and systematic testing of four M06-class functionals and 12 other functionals, Theor. Chem. Acc., 120, 215-241, https://doi.org/10.1007/s00214-007-0310-x, 2007.
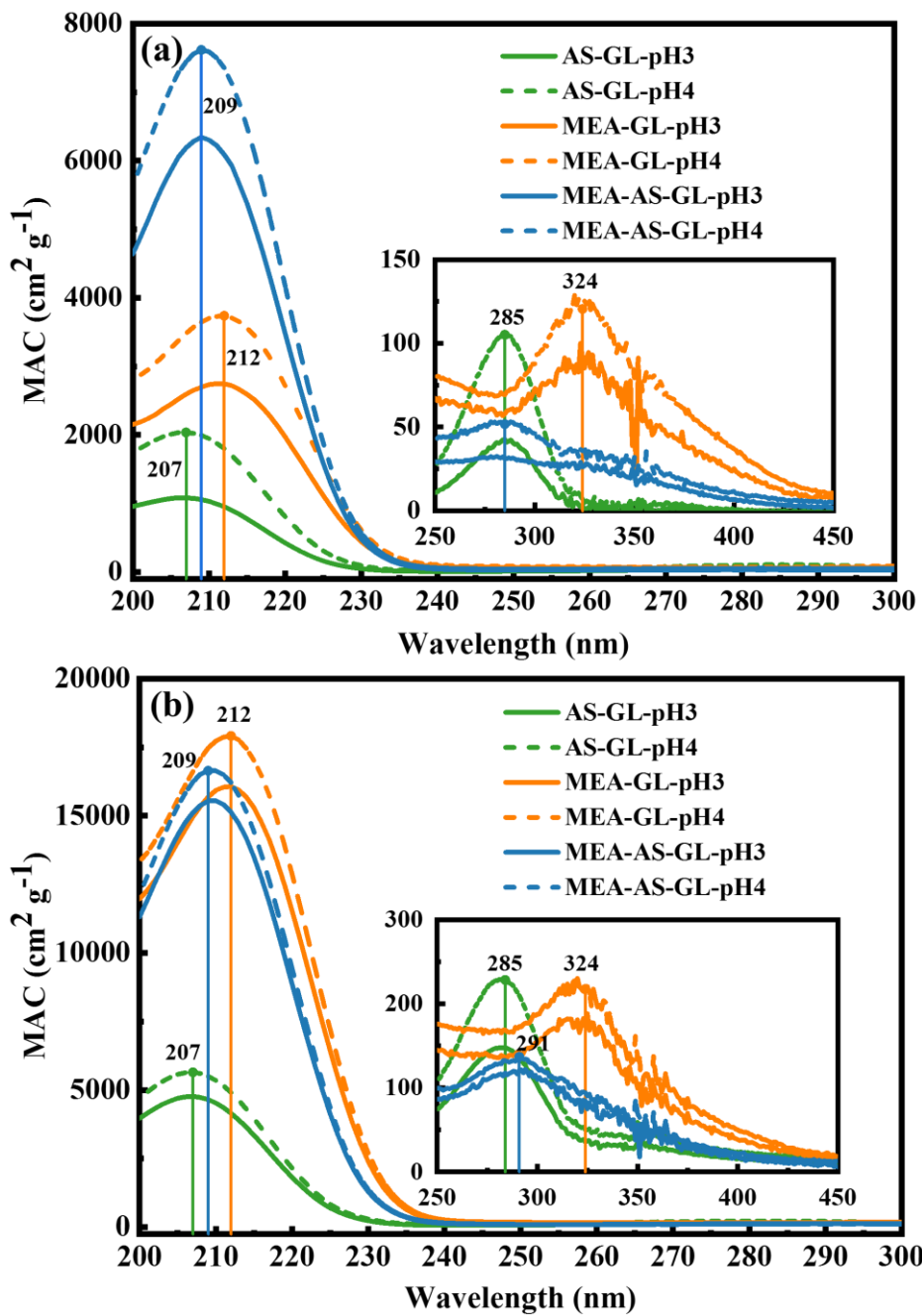
Figure 1: The MAC values for AS-GL, MEA-GL and MEA-AS-GL mixtures at the initial pH of 3 and 4 at 1d (a) and 15d (b).

541
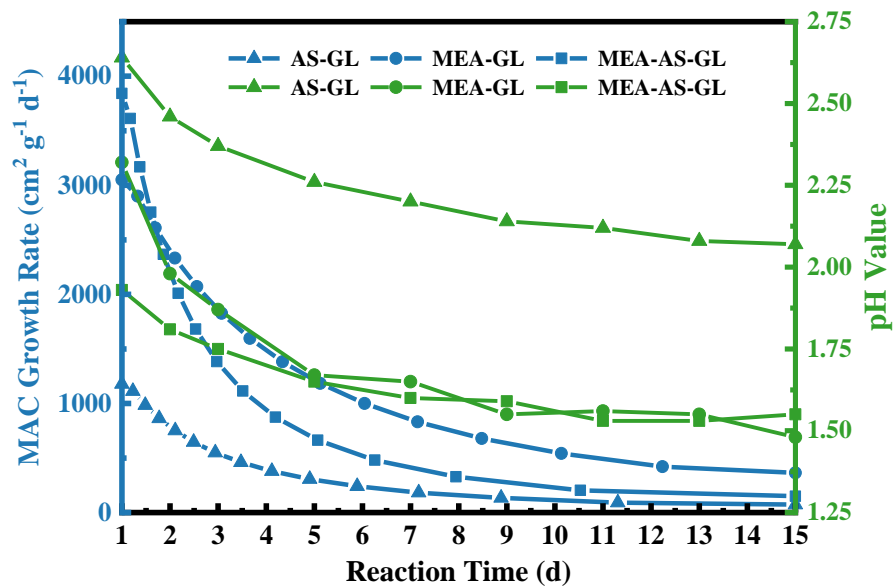
Figure 2: Dependence of the growth rates (blue line) and pH values (green line) on reaction time for AS-GL, MEA-GL and MEA-AS-GL mixtures.
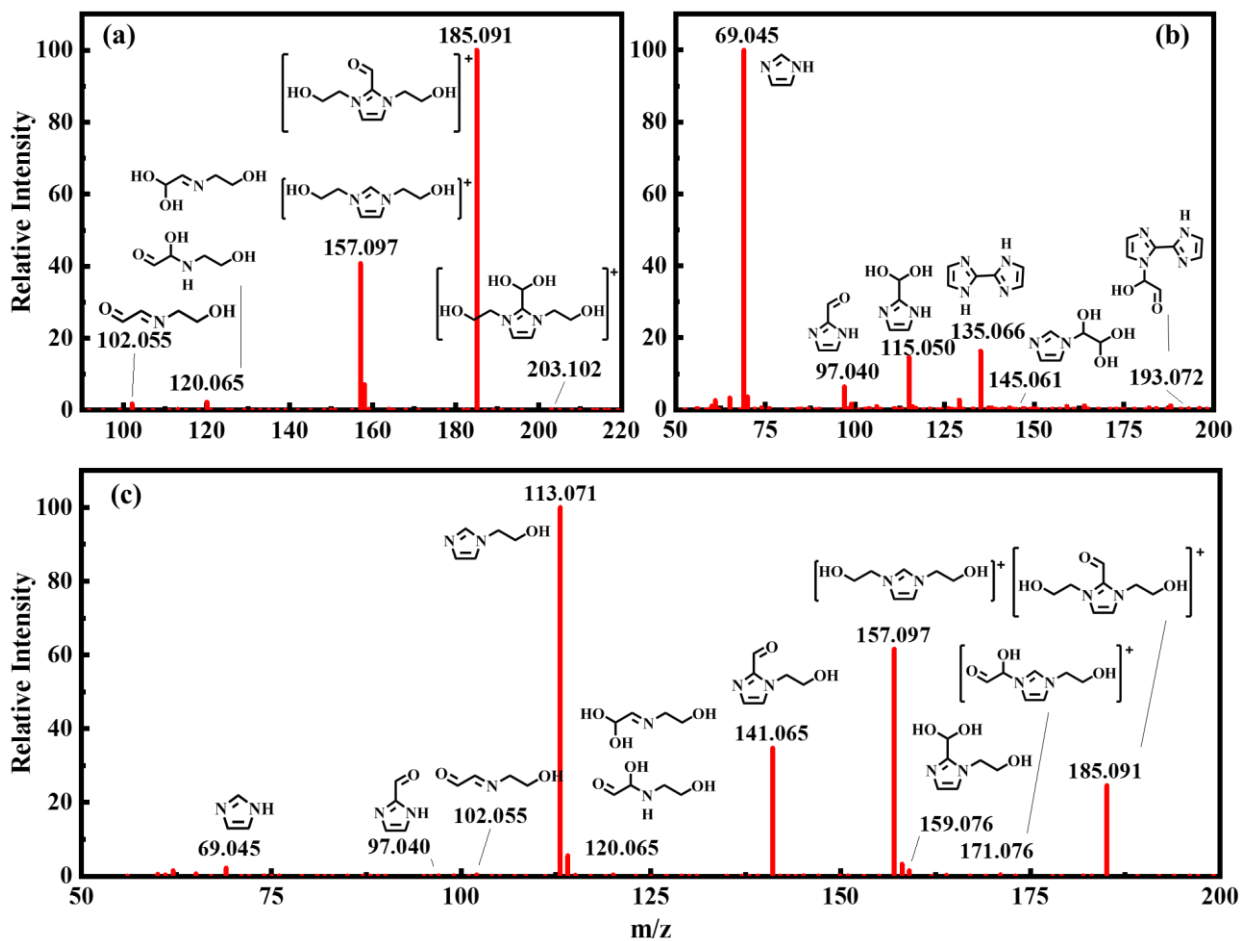
Figure 3: Mass spectra monitoring of chromophores for (a) MEA-GL (b) AS-GL and (c) MEA-AS-GL mixtures.
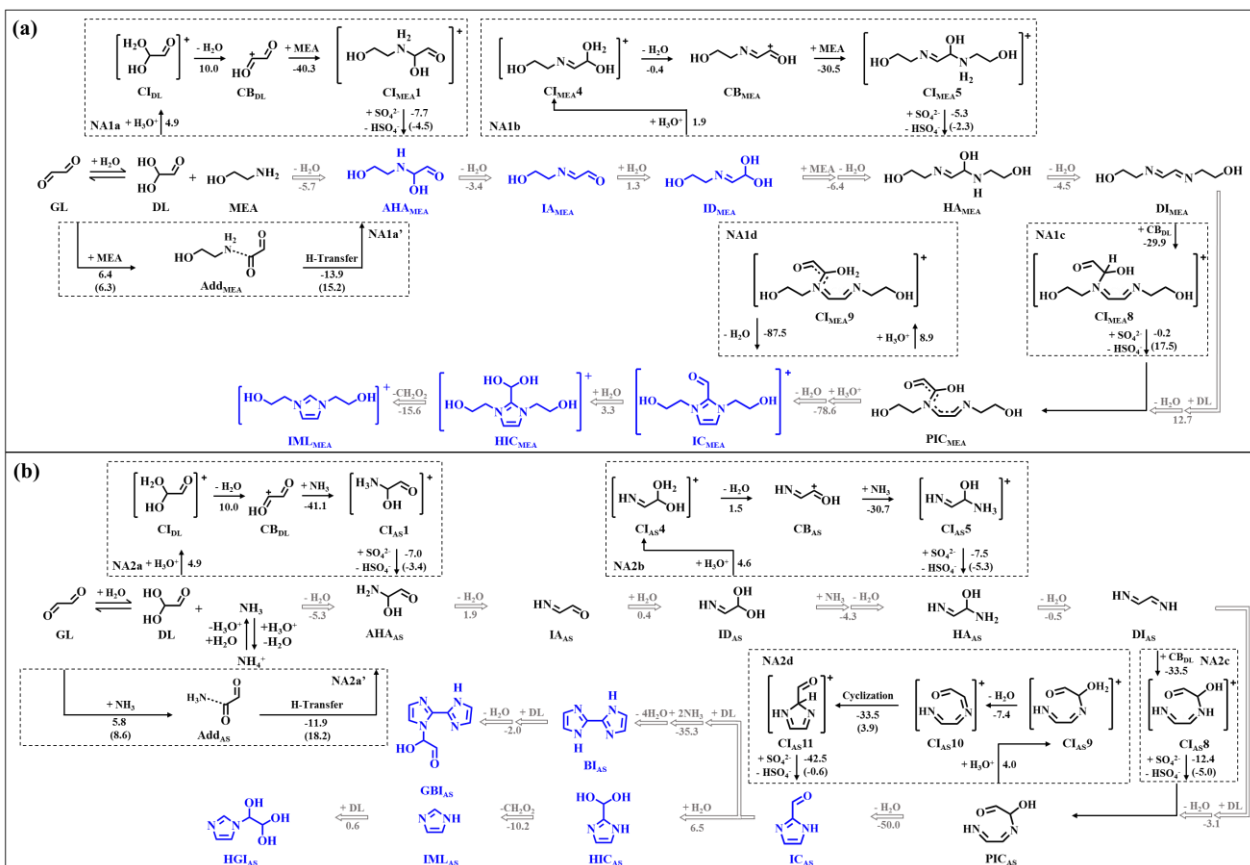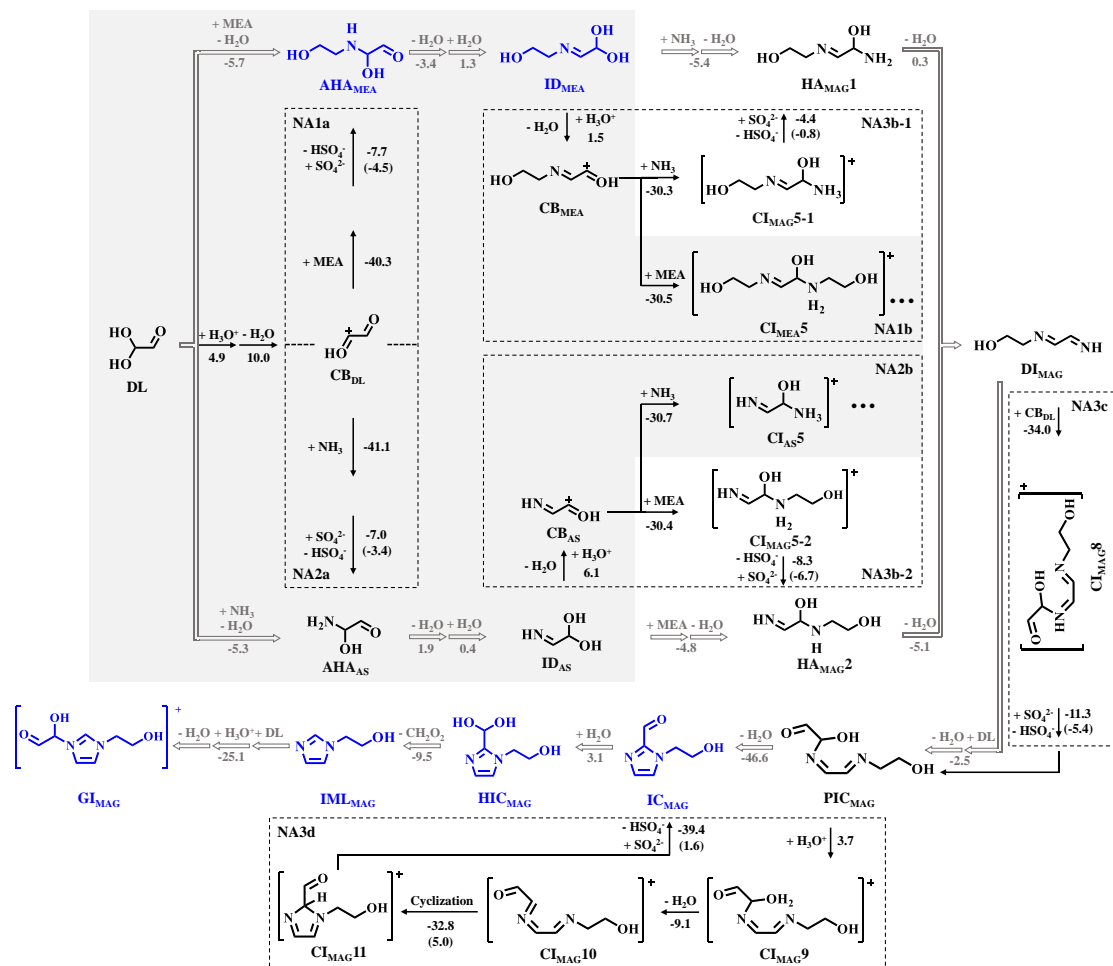
544

545

Figure 4: Possible pathways leading to chromophores for (a) MEA-GL and (b) AS-GL mixtures (oriented by gray arrows). Detailed PESs of the four NA reactions are presented in dotted boxes. The number denotes the values of ΔG_r and $\Delta G^{\ddagger}$ (in brackets) for each reaction step (in kcal mol^{-1}), and all energies are relative to the corresponding reactants.

Figure 5: Possible pathways leading to chromophores for MEA-AS-GL mixture (oriented by gray arrows). Detailed PESs of the four NA reactions are presented in dotted box. The shaded area is the overlapping part with the pathways of MEA-GL and AS-GL mixtures. The number denotes the value of ΔG_r and $\Delta G^\ddagger$ (in brackets) for each reaction step (in kcal mol^{-1}), and all energies are relative to the corresponding reactants.